

Check for updates

Minimizing Inter-Lattice Strain to Stabilize Li-Rich Cathode by Order-Disorder Control

Shenyang Xu, Zhihai Gao, Hao Chen, Liang Chang, Nian Zhang, Dong Zhou, Tianyi Li, Tony Wang, Cong Lin, Haoyu Xue, Qinghao Lai, Weiyuan Huang, Luyi Yang, Jiajie Liu, Tongchao Liu, Lunhua He, Mingjian Zhang,* Zhengyan Lun,* and Feng Pan*

Li-rich Mn-based layered (LMR) cathodes with anionic redox chemistry show great potential for next-generation sustainable Li-ion battery (LIB) applications due to the low cost and high energy density. However, the asynchronous structural evolutions with cycling in the heterogeneous composite structure of LMR lead to serious lattice strain and thus fast electrochemical decay, which hinders the commercialization of LMR cathodes. Here, an order-disorder coherent LMR cathode is demonstrated that exhibits a higher average voltage (by 0.25 V), negligible voltage decay (97.6% voltage retention after 100 cycles at 100 mA g⁻¹), and enhanced cycling stability (98% capacity retention after 200 cycles at 100 mA g⁻¹) compared to its layered oxide counterparts. It is proposed that this order-disorder coherent structure design can promote a more synchronous and homogeneous structure evolution during charge and discharge, thus minimizing lattice strain, which significantly prevents layer collapse and collective degradation at high voltage, improving the electrochemical stability. The study displays the feasibility of optimizing the performance of Li-rich cathode materials through a dedicated order-disorder structure control for sustainable energy storage.

1. Introduction

The rapidly growing Li-ion battery (LIB) industry is accelerating the pursuit of sustainable cathodes with low-cost and high energy density. LMR is a promising class of nextgeneration cathode material, which typically adopts an O3-type structure and can be described as Li₂MnO₃·LiTMO₂ (TM=Ni, Co, Mn, Al, etc.). LMR cathodes exhibit high energy density relying on both cationic and anionic redox chemistry.^[1,2] However, the commercialization of LMR is hindered by voltage and energy decay, which have been correlated with TM migration and irreversible structural degradation.^[3]

Understanding the structural origin of electrochemical decay within O3-type LMR is crucial for performance improvement. The lattice strain in a heterogeneous composite structure is a primary cause of the structural degradation in LMR cathodes.^[4]

S. Xu, Z. Gao, H. Xue, Q. Lai, L. Yang, J. Liu, F. Pan School of Advanced Materials Shenzhen Graduate School Peking University

Shenzhen 518055, China E-mail: panfeng@pkusz.edu.cn

H. Chen, Z. Lun

School of Chemical Sciences

 $University of Chinese \, Academy \, of \, Sciences \,$

Beijing, China

E-mail: zylun@ucas.ac.cn

L. Chang

Institute of Materials Research

Tsinghua Shenzhen International Graduate School

Tsinghua University Shenzhen 5 18055, China

N. Zhang

China Shanghai Synchrotron Radiation Facility Shanghai Advanced Research Institute

Chinese Academy of Sciences Shanghai 201204, China

The ORCID identification number(s) for the author(s) of this article can be found under https://doi.org/10.1002/adma.202418580

DOI: 10.1002/adma.202418580

D. Zhou

Institute of Advanced Science Facilities

Shenzhen 518107, China

T. Li

X-Ray Science Division

Argonne National Laboratory

Lemont, IL 60439, USA

W. Huang, T. Liu

Chemical Sciences and Engineering Division

Argonne National Laboratory

Lemont, IL 60439, USA

T. Wang

Central Analytical Research Facility

Institute for Future Environments

Queensland University of Technology

2 George Str., Brisbane, Queensland 4000, Australia

C. Lin

Department of Applied Biology and Chemical Technology

The Hong Kong Polytechnic University

Kowloon, Hong Kong SAR 999077, China

L. He

China Spallation Neutron Source Dongguan 523803, China

M. Zhang

School of Science and Engineering

The Chinese University of Hong Kong Shenzhen, Guangdong 518172, China E-mail: zhangmingjian@cuhk.edu.cn

1521495, 2025, 32, Downloaded from https://dvanced online library.wiely.com/doi/10.1002adma.020418580 by University Town Of Shenzhen, Wiley Online Library on [16/11/0205]. See the Terms and Conditions (https://onlinelibrary.wiely.com/terms-and-conditions) on Wiley Online Library for rules of use; OA archies are governed by the applicable Centwise Commons I

The two-layered phase components (S. G. *R-3m* and *C2/m*) typically exhibit an uneven distribution within the lattice, resulting in asynchronous and heterogeneous structural evolutions during charge—discharge.^[5] These heterogeneous structural evolutions generate serious lattice strain at the interphasic regions and the unidirectional stretching around deconstructed defects, which induce the irreversible TM migration and accelerate the structural and electrochemical fading at high voltage,^[4,6–9] In brief, the structural complexity of traditional LMR cathodes result in significant strain non-uniformity and structural instability,^[4,10] hindering their commercial application. Addressing the challenge through mitigating the unidirectional and continuous strain could lead to a structurally stable LMR cathode.^[11]

While conventional approaches like cation doping, surface engineering, and phase structure control have been employed to enhance the electrochemical performance of LMR cathodes, these methods do not seem to be rationalized for manipulating the reaction heterogeneity and lattice strain during cycling. [1,3,4,12–14] In comparison to commercial LIB cathodes such as lithium cobalt oxide and nickel based oxide, which show more homogeneous reactivity and reversible redox process with smaller lattice strain and moderate kinetics regardless of the participation of oxygen redox, LMR cathodes typically exhibit sluggish and asymmetric redox process, [15–18] hypothesized to be a consequence of a kinetic perspective arising from the aforementioned structure heterogeneity. Deciphering the complex kinetics of LMR cathodes to achieve homogeneous reactivity and mitigated lattice strain remains a formidable challenge.

In this work, an order–disorder coherent LMR cathode was designed to mitigate the heterogeneous strain and collective structure degradation. In combination of synchrotron X-ray diffraction (XRD) and neutron diffraction (ND), high-angle annular dark-field scanning transmission electron microscopy (HAADF-STEM), time-of-flight secondary ion mass spectrometry (ToF-SIMS), and soft X-ray absorption spectroscopy (sXAS), we have decoupled the complex evolution of structural and chemical states in O3-type LMR with superior electrochemical stability. The enhanced electrochemical performance is attributed to the disruption of single directional stretching by order–disorder nanodomain, thereby achieving homogeneous lattice strain during cycling, implying an effective optimization pathway for advanced O3-type LMR materials.

2. Results

2.1. Architecting Order-Disorder Coherent Structure

The structural heterogeneity of the LMR cathode exacerbates local structural rearrangement during cycling. [4,5] Prolonged cycling induces irreversible TM migration, which converts 1-TM channels into 2-TM channels within the Li⁺ percolation network (Figure S1, Supporting Information). [19] This migration leads to the formation of dispersed antisite defects with TM ions occupying Li sites that obstruct Li⁺ diffusion channels and create areas of high lattice strain, ultimately resulting in increased structural degradation (Figure 1a). To address this, we propose to construct localized coherent disordered nano-domains through which Li⁺

percolation occurs through a "0-TM" network. [19] The key difference between the two scenarios is that in the former case, the bulk antisite defects are isolated and dispersed within the layered matrix at an atomic scale; in contrast, in the latter one, the cation disorder appears in a larger length scale to form disordered nano domains with a coherent anion framework. Even when certain Li+ diffusion channels become blocked, the disordered domains can function as buffers, enabling the reconfiguration of Li+ diffusion pathways. This strategy is expected to effectively mitigate lattice strain during cycling, thereby enhancing the sustainability of LMR cathodes.

The feasibility of this material design strategy was evaluated in a fluorinated LMR cathode $\mathrm{Li}[\mathrm{Li}_{0.25}\mathrm{Mn}_{0.5}\mathrm{Ni}_{1/6}\mathrm{Al}_{1/12}]\mathrm{O}_{2-x}\mathrm{F}_{x}$, denoted as LMNAF. Here F-to-O substitution was applied to promote the formation of disordered nano domains, taking advantage of the affinity between Li and F. In Figure 1b, we present the calculated formation energy (per atom) of various structures with the traditional composition (Li[Li $_{\!1/4}Mn_{1/2}Ni_{1/6}Al_{1/12}]O_{1.75}F_{0.25})$ as a function of the average number of Li-F bonds formed around a F atom. The calculated energy values are averaged over 48 different structures, with computation details described in the Experimental Section. Notably, the formation energy decreases with an increasing average number of Li ions surrounding each F ion. This trend can be attributed to the fact that the formation of TM-F bonds, as the average number of Li-F bonds per F ion decreases, necessitates a higher energy that is typically unattainable. Consequently, the presence of F ions within the lattice can promote the formation of Li+ rich local environments. Furthermore, according to Pauling's principle of electroneutrality, TMs located near F ions are likely to occupy different layers, resulting in a localized disordered nanodomain.

The order-disorder coherent cathode LMNAF can be successfully synthesized via a sol-gel method in O2 atmosphere. For comparison, Li-rich layered material Li[Li_{0.25}Mn_{0.5}Ni_{1/6}Al_{1/12}]O₂ (LM-NAO) was synthesized. As shown in Figure 1c,d and Figures S2, S3 (Supporting Information), LMNAF and LMNAO were structurally characterized by synchrotron XRD and ND. A joint Rietveld refinement indicates that both LMNAF and LMNAO show similar ratios between rhombohedral R-3m and monoclinic C2/m phases, but LMNAF exhibits a higher level of Li/TM (TM=Mn, Ni, Al) disordering of ≈3.78% with larger lattice parameters compared to 0% for LMNAO (Tables \$1, \$2, Supporting Information)[20,21] Scanning transmission electron microscopy (STEM) and energy-dispersive X-ray spectroscopy (EDX) results of LMNAF sample, presented in Figure 1e, confirm a homogeneous distribution of Ni, Mn, Al, O, and F. The high-resolution transmission electron microscopy (HRTEM) and selected area electron diffraction (SAED) pattern confirm the composite nature of LMNAF particles composed of nanosized coherent disordered domains within a particle (Figure 1f,g; Figure S4, Supporting Information). To further evaluate the short-range structure, X-ray total scattering coupled with pair distribution function (PDF) was acquired and displayed in Figure \$5 (Supporting Information). The results show larger lattice parameters of LM-NAF (Tables S3, S4, Supporting Information), consistent with the joint refinement results. The structural characterizations demonstrate the order-disorder coherent feature in the LMNAF compound.

ununu advimat da

1521 4095, 2025, 32, Downloaded from https://advanced.onlinelibrary.wiley.com/doi/10.1002/adma.202418580 by University Town Of Shenzhen, Wiley Online Library on [16/11/2025]. See the Terms

ınd-conditions) on Wiley Online Library for rules of use; OA articles are governed by the applicable Creative Commons

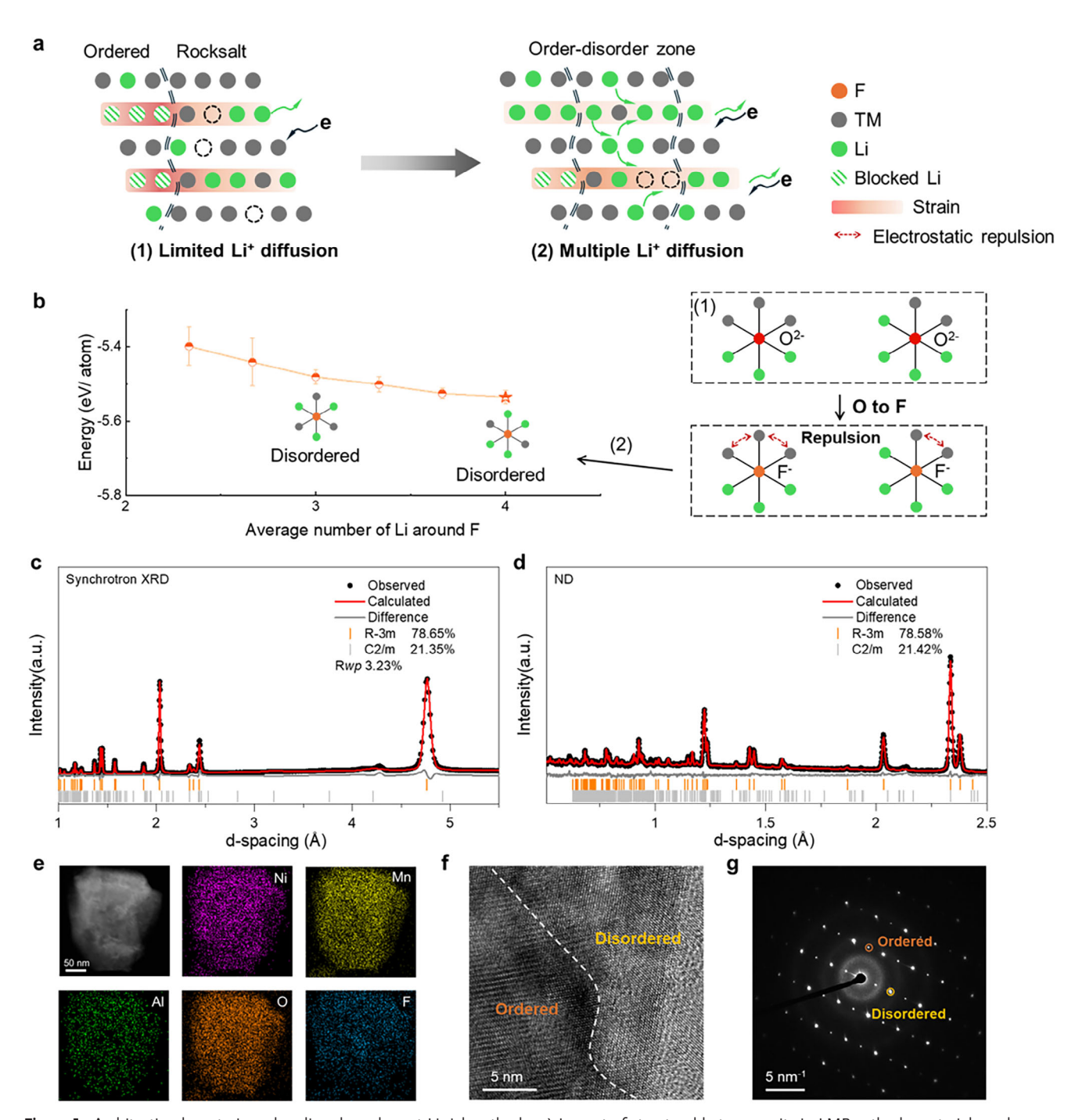


Figure 1. Architecting low-strain order–disorder coherent Li-rich cathode. a) Impact of structural heterogeneity in LMR cathode materials and reconfiguration of Li⁺ diffusion pathways by introducing disordered "buffer". b) DFT calculations of formation energy to prove the feasibility of introducing disorder in LMR cathodes. c,d) Synchrotron XRD (c) and ND (d) of LMNAF and the combined Rietveld refinement (Li/TM disordering ratio: 3.78%). e) STEM image and EDX mapping of the elements Ni, Mn, Al, O, and F. f) HRTEM image of order–disorder domain in LMNAF. g) SAED pattern of as-synthesized LMNAF.

2.2. Improved Electrochemistry

The coherent order–disorder structure further contributes to improved electrochemical performance. The electrochemical performance of LMNAF and LMNAO was first analyzed in a galvanostatic mode at a current density of 20 mA $\rm g^{-1}$ within a volt-

age window of 2–4.8 V as shown in Figure S6 (Supporting Information). Notably, LMNAF exhibits a superior discharge capacity of 229.0 mAh g⁻¹, surpassing that of LMNAO, which delivers a comparatively lower discharge capacity of 195.9 mAh g⁻¹. Crucially, a higher average voltage is maintained for LMNAF during the discharge process, with an elevation in the discharge average

1521495, 2025, 32, Dwnholoded from https://dvnnced.oninlib/arry.wiley.com/doi/10.1002/adm.202418580 by University Town Of Sherazhen, Wiley Online Library on [16/11/12/5], See he Terms and Conditions (https://onlinelibrary.wiley.com/terms-and-conditions) on Wiley Online Library for rules of use; OA articles are governed by the applicable Cerative Commons

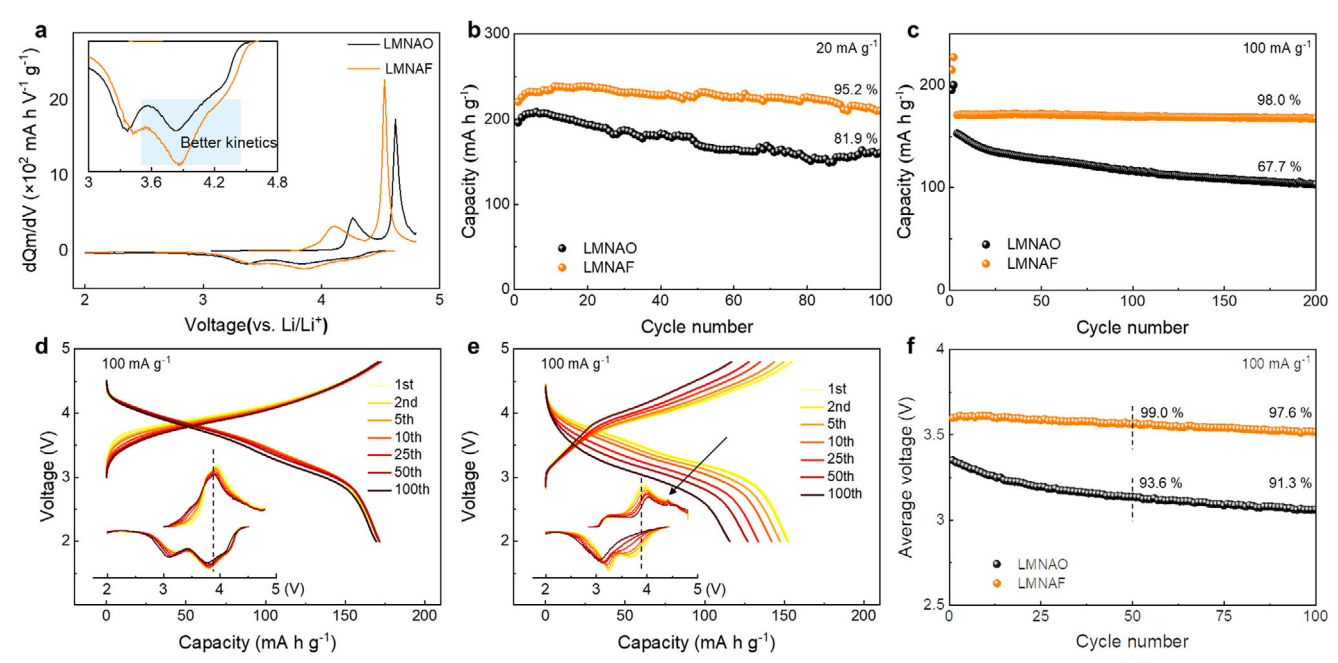


Figure 2. Electrochemical performance of LMNAF and LMNAO. a) The corresponding differential capacity (dQm/dV) curves of the first cycle. b,c) Long cycle stability at the current densities of 20 mA g^{-1} (b) and 100 mA g^{-1} (c). d,e) The capacity-voltage profiles at 1st, 2nd, 5th, 10th, 25th,50th, 100th cycle of LMNAF (d) and LMNAO (e) after 3 cycles' activation at 20 mA g^{-1} . Inserts are the corresponding dQm/dV profiles, and the *x*-axis represents voltage. f) The average voltage of LMNAF and LMNAO at the current densities of 100 mA g^{-1} .

voltage from 3.55 V for LMNAO to 3.69 V for LMNAF, indicating an enhancement in energy density. Differential capacity (dQm/dV) analysis (shown in Figure 2a) reveals an earlier onset of redox activity involving both TM and oxygen redox in LM-NAF during initial charge. [7,22,23] The elevated average voltage in LMNAF is primarily attributed to a more pronounced contribution from oxygen redox. During the discharge process, LMNAF exhibits enhanced kinetics with more capacity contribution at higher voltage, resulting in a reduced voltage hysteresis, in sharp contrast to conventional Li-rich layered cathode materials.[14,24-26] As shown in Figure S7 (Supporting Information), LMNAF maintains better kinetics in subsequent cycles, as evidenced by a more reversible charge-discharge redox behavior. After 50 cycles, the discharge profile of LMNAF shows less voltage hysteresis (Figure S8, Supporting Information).[14,27-29] The cyclability of LMNAF is also greatly improved with a higher capacity retention of 95.2% after 100 cycles at 20 mA $\rm g^{-1}$ and 98.0% after 200 cycles at 100 mA g⁻¹, as compared to LMNAO, which exhibits 81.9% and 67.7% capacity retention under the same cycling conditions, respectively (Figure 2b,c). Figure 2d-f further illustrates the enhanced performance at high current density with a slower voltage decay and improved kinetics during cycling. Figure 2d shows the enhanced kinetics of LMNAF, notably featuring nearly ignorable voltage decay during cycling. This is a significant deviation from the conventional behavior observed in traditional Li-rich materials. In contrast, LMNAO exhibits the typical voltage decay commonly observed in such materials (Figure 2e). Remarkably, LM-NAF demonstrates a voltage retention of 97.6%, with a marginal decrease from 3.60 to 3.52 V after 100 cycles. In contrast, LM-NAO exhibits a lower retention rate of 91.3%, with its voltage diminishing from 3.35 to 3.06 V (Figure 2f). The electrochemistry

demonstrates the higher energy density and longer-term cycling stability of LMNAF.

2.3. Enhanced Structural Robustness

The structure stability upon extended cycling was investigated using HAADF-STEM, synchrotron XRD, sXAS and ToF-SIMS to further understand the highly enhanced cycling retention and superior kinetics of LMNAF. In Figure 3a, HAADF-STEM analysis and its corresponding fast Fourier transform (FFT) of LMNAF at 4.8 V distinctly reveal an intergrown structure, composed of disordered and ordered (layered) nano domains. No discernible interphase boundaries can be observed, presumably because of a coherent anion lattice framework, critical to maintaining high Li ion mobility across domain boundaries. These structural features are almost identical to those presented at a pristine state (Figure 1g), demonstrating the excellent stability of this intergrown structure at 4.0, 4.4 and even up to 4.8 V (Figures S9, S10, Supporting Information; Figure 3a), without observable lattice displacements which are common for conventional LMR cathodes even at a lower voltage.^[4] In contrast, LMNAO exhibits significant distortion at 4.4 V (Figure S11, Supporting Information). This demonstrates the role of order-disorder coherent domains in enhancing structural resilience against stress, as confirmed by the results of geometric phase analysis (GPA)[30] showing negligible lattice mismatch between the ordered and disordered domains in electrochemical reactions. In the majority of the ordered regions, as depicted in Figure 3b, the coherent lattice structure is retained without interlayer TM migration. And an increased layer spacing of 4.87 Å is observed, attributable primarily to the

15214095, 2025, 32, Downloaded from https://adv

.com/doi/10.1002/adma.202418580 by University Town Of Shenzhen, Wiley Online Library on [16/11/2025]. See the Terms

on Wiley Online Library for rules of use; OA articles are governed by the applicable Creative Common

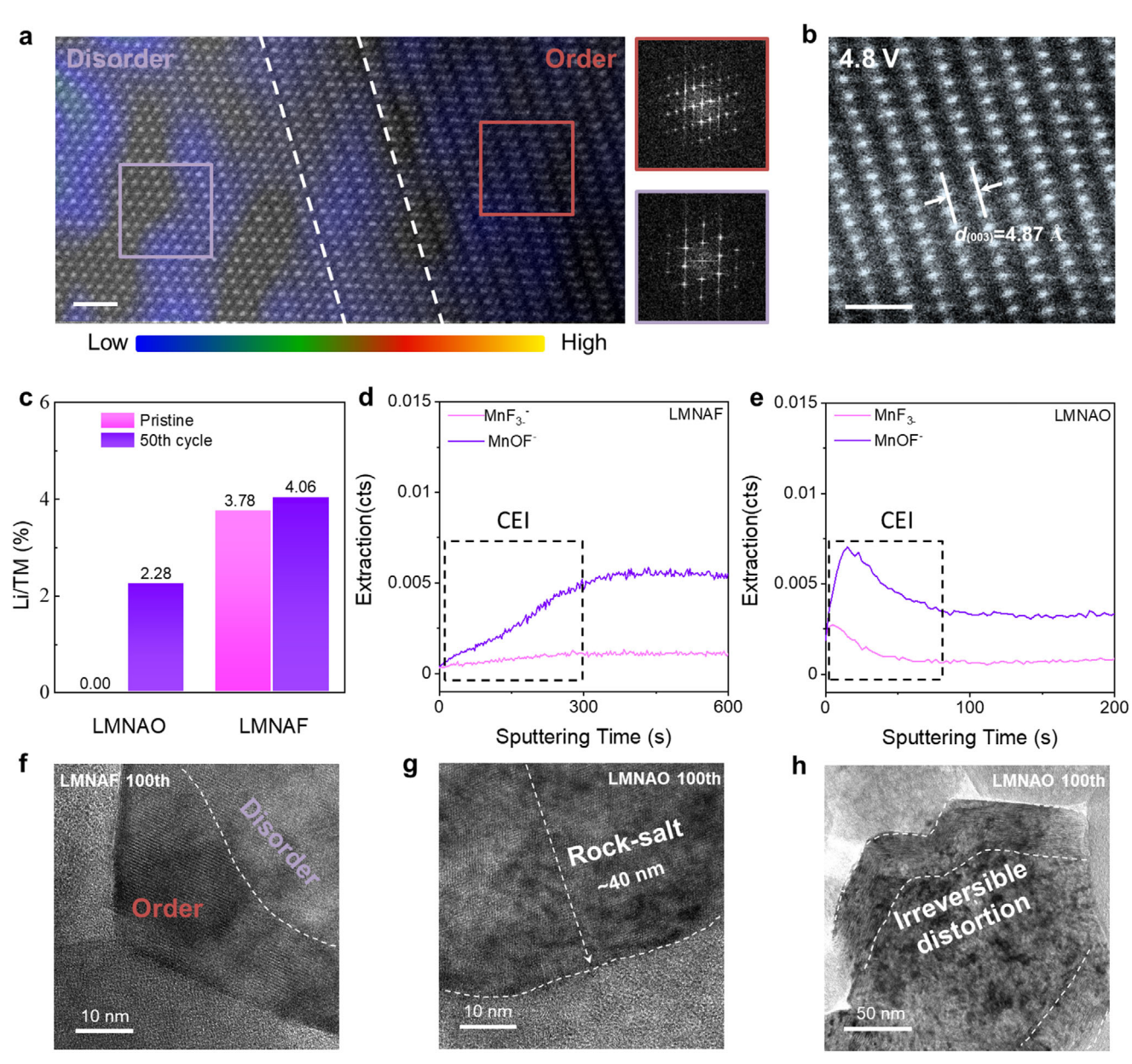


Figure 3. Bulk and surface structure change. a,b) STEM-HAADF images showing the composite phase (a) and perfect layered phase (b) of LMNAF after charging to 4.8 V. The scale bar is 1 nm. The strain analysis between ordered and disordered domains is conducted by GPA. c) Li/TM antisite concentrations in LMNAO and LMNAF before cycling and after the 50th cycle obtained from the corresponding synchrotron XRD Rietveld refinement results. d,e) ToF-SIMS characterization of the material surface after 50 cycles for LMNAF cathode (d) and LMNAO cathode (e), showing MnF₃⁻ and MnOF⁻ ions, respectively. The composition of the cathode electrolyte interface (CEI) is delineated in Figure S14 (Supporting Information). f) HRTEM images of LMNAF after 100 cycles. g,h) HRTEM images of LMNAO after 100 cycles: surface degradation (g) and irreversible distortion (h).

increase in repulsion between oxygen layers as a result of extensive ${\rm Li^+}$ extraction from the alkali layer (Figure S12, Supporting Information).^[4]

A more bulk-sensitive evaluation of the structural stability upon cycling was conducted by synchrotron XRD Rietveld refinement of the pristine (before cycle) and aged (50th cycle) materials (Figure 3c; Figure S13 and Table S5, Supporting Information). The accumulation of antisite defects during cycling is deemed detrimental. These antisite defects are isolated and dispersed (i.e., without forming rock-salt local domains), which can

not function to perturb collective degradation but may impede the Li⁺ migration. An increase in Li/TM disordering serves as an indicator of macro structural degradation during cycling. LM-NAF exhibits a negligible increase in Li/TM disordering, with only 0.22%, in contrast to the 2.28% increase observed for LM-NAO. These effects can be attributed to the introduction of coherent disordered domains, which promote uniform strain distribution, thereby preventing continuous structural degradation and reducing TM migration. Besides better bulk reversibility, LM-NAF also presents enhanced surface stability, which may also

1521495, 2025, 32, Downloaded from https://dvanced online library.wiely.com/doi/10.1002adma.020418580 by University Town Of Shenzhen, Wiley Online Library on [16/11/0205]. See the Terms and Conditions (https://onlinelibrary.wiely.com/terms-and-conditions) on Wiley Online Library for rules of use; OA archies are governed by the applicable Centwise Commons I

contribute to its cycle life. sXAS at Mn L-edge in the total electron yield (TEY) mode reveals that the valence state of Mn remains constant throughout the 1st cycle of LMNAF (Figure \$15, Supporting Information), but a larger fraction of Mn³⁺ present at the surface of LMNAO. [31] ToF-SIMS and X-ray photoelectron spectroscopy (XPS) measurement was also conducted to examine the TM dissolution after 50 cycles (Figure 3d,e; Figure S16, Supporting Information), which suggests the mitigated TM dissolution in LMNAF. Long-term cycling induced strain accumulation after 50 and 100 cycles further highlights the superior structural stability of LMNAF. HRTEM analysis after 50 cycles reveals that LM-NAF retains its coherent order-disorder structure with negligible distortion, whereas LMNAO develops dispersed antisite defects (Figures S17, S18, Supporting Information). After 100 cycles, LMNAF continues to exhibit a coherent order–disorder structure, while LMNAO undergoes severe degradation, evidenced by irreversible lattice distortion and the formation of a thick rock-salt surface layer (Figure 3f-h). These contrasts underscore the pronounced strain accumulation in LMNAO, ultimately leading to cathode failure.

2.4. Formulating the Homogeneous Redox Mechanism

To further understand the redox process of LMNAF, in situ XRD and ex situ sXAS under the TEY mode and total fluorescence yield (TFY) mode were performed. The in situ XRD results highlight a significant difference in the evolution of the superlattice feature between LMNAF and LMNAO during cycling, as shown in Figure 4a and Figures S19, S20 (Supporting Information). The intensity of the superlattice feature typically decreases upon charging to high voltage for typical Li-rich Mn-based cathodes,[4] which is also observed for LMNAO. The sharp decrease in the superlattice peak above 4.5 V suggests the disruption of collective TM ordering.^[4] In contrast, the superlattice in LMNAF remains almost unchanged after two cycles. This demonstrates that the TM ordering is well-preserved and that intralayer or interlayer TM migration is mitigated. Moreover, Li+ extraction adjacent to Mn in the TM layer is largely suppressed, which would otherwise lead to a reduction in the superlattice peak.^[4] Instead, this indicates that during charging, Li ions in the alkali layers are preferably removed. This evolution of the superlattice peak feature demonstrates negligible strain during cycling.

Furthermore, Mn L-edge, Ni L-edge, O K-edge, and F K-edge sXAS under a bulk-sensitive TFY mode were conducted to monitor changes in the oxidation states. The sXAS spectra for Mn and Ni L-edges can be categorized into two distinct regions: the L_3 -edge at a lower photon energy and the L_2 -edge at a higher energy, a differentiation resulting from the spin-orbit splitting of the 2p core hole. The almost invariant spectra observed at the Mn L_3 -edge throughout the 1st cycle of LMNAF and LMNAO confirm that Mn⁴⁺ remains electrochemically inactive (Figure 4b), and the variation in the intensity of L_2 -edge change is related to the $2p^{1/2}$ orbital local environment change. Target S21, Supporting Information). S23, S43 caused by O-K emission (Figure S21, Supporting Information).

Figure S22 (Supporting Information), both the Ni L_3 and the L2-edge sXAS distinctly demonstrate a shift in spectral weight toward higher energy. Specifically, during the delithiation process, feature 1 (F1) decreases and feature 2 (F2) increases, suggesting a correlation with the modulation of Ni oxidation states. This trend is characterized by an increase in Ni oxidation during delithiation. Conversely, during lithiation, F1 increases and F2 decreases, corresponding to a reduction in Ni oxidation states, which has been demonstrated to be beneficial to long-term cycling stability.[37-39] The sXAS analysis reveals that pristine LM-NAF exhibits a slightly lower Ni valence state compared to LM-NAO, attributed to the fluorination synthesis process. This fluorination helps maintain charge neutrality and induces the formation of disordered domains. It is also observed that Ni ions in LMNAO are oxidized to a higher oxidation state at high voltage than those in LMNAF, but achieve a lower capacity, which may also be attributed to the inhomogeneous lattice strain. In Figure 4b,c, the Mn and Ni L-edge peak features of LMNAO are intensified at 4.8 V compared to LMNAF, accompanied by a shift to higher energy. This increase in intensity reflects the formation of Mn and Ni vacancies, corresponding to an increase in Mn and Ni 3d orbital holes.^[40] This phenomenon can be attributed to TM migration, which is consistent with the local structural changes at high voltage observed by HAADF-STEM in Figure 3a,b.

The O K-edge sXAS spectra can be primarily divided into a pre-edge region and a broad band (Figure 4d). The pre-edge region originates from the electron transitions of O_{1s} to TM_{3d}-O_{2n} hybrid orbitals, while the broad band is attributed to the electron transition from O_{1s} to TM_{4sp} - O_{2p} primarily influenced by the coordination environment. [23,41,42] Upon charging, an additional shoulder peak emerges at \approx 530.5 eV, marked by the dashed line in Figure 4d, indicating the presence of oxidized oxygen species with more O_{1s} core electrons. Notably, LMNAF displays a more pronounced peak at ≈530.5 eV compared to LMNAO when charged to 4.8 V. This suggests a larger contribution from oxygen redox in LMNAF, contributing to its higher capacity. This higher capacity of LMNAF is also more reversible in subsequent cycles, as shown in Figure 4e. The enhancement of the peak preceding the dashed line can be ascribed to the rehybridization between the TM and O ions. This rehybridization results in a distortion of their local structure, thereby generating a higher effective nuclear charge at the metal ions. [41,43] The pre-edge is indicative of the distribution of oxygen hole states above the Fermi level. Although the modified sample contains more oxygen holes, the emitted electrons from oxygen are captured by the (TM-O)* band rather than leading to O₂ release, as demonstrated by operando differential electrochemical mass spectrometry (DEMS) (Figure S23, Supporting Information). In the 2nd cycle, the peaks of LMNAO decrease and become irreversible during charging, suggesting that the structural distortion in the LMNAO sample is irreversible during cycling due to the intrinsic structural arrangement. [44] In Figure 4f, investigation on the F K-edge spectra confirms the presence of F species in all the cycling processes. The similarity in the sXAS results indicates a stable chemical state throughout the processes, $^{[45,46]}$ suggesting that the local structural characteristics of F remain unaltered and most of the F resides in disordered domains.

15214095, 2025, 32, Downloaded from https://advancec

onlinelibrary.wiley.com/doi/10.1002/adma.202418580 by University Town Of Shenzhen, Wiley Online Library on [16/11/2025]. See the Terms

and-conditions) on Wiley Online Library for rules of use; OA articles are governed by the applicable Creative Commons

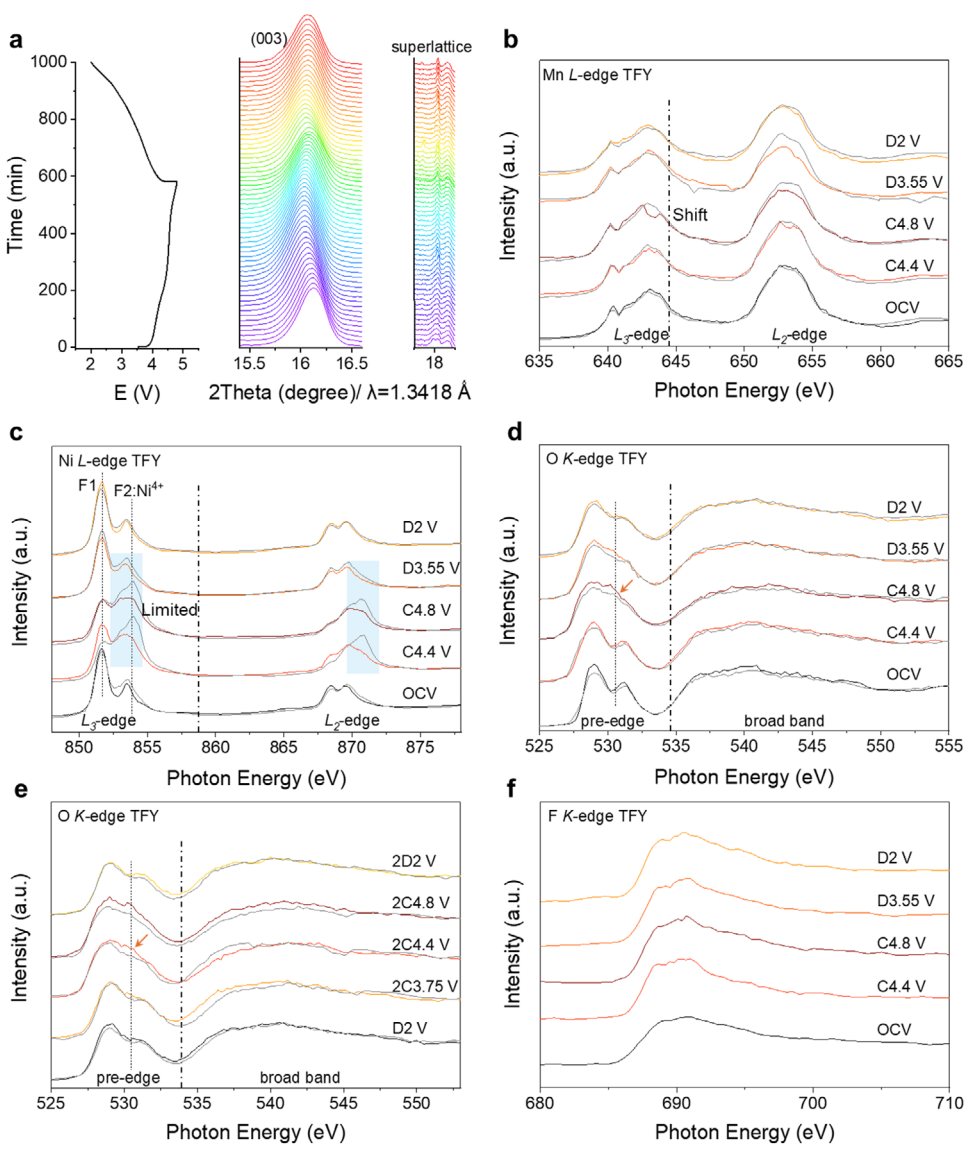


Figure 4. Structural and chemical changes. a) In situ synchrotron XRD patterns showing the evolution of the (003) peak and superlattice peaks of LMNAF cathodes at different states of the 1st cycle. b–d) sXAS at the Mn *L*-edge (b), Ni *L*-edge (c), and O *K*-edge (d) of LMNAF (colored lines) and LMNAO (grey lines) under TFY mode at different states of the 1st cycle. e) O *K*-edge sXAS under TFY mode at different states of the 2nd cycle. f) F *K*-edge sXAS spectra of LMNAF under TFY mode at different states of the 1st cycle.

3. Discussion

To better understand the kinetic origin of the improved electrochemical performance, we applied electrochemical impedance spectra (EIS) and distribution of relaxation time (DRT) analysis. DRT analysis can examine charge transfer kinetics related to the electrochemical reaction by timescale identification (Figure 2a,b). [47] The charge transfer resistance of LMNAF is smaller than that of LMNAO, indicating better diffusion kinetics. The large differences in response time, especially at the end of charge, reflect the impeded charge transfer of LMNAO at $\approx\!4.8~\rm V$. In long-term cycling, EIS for LMNAF and LMNAO in Figure S24 (Supporting Information) present Nyquist plots that delineate the kinetic behaviors. During cycling, LMNAF shows lower

resistance than LMNAO (Figure S25, Supporting Information). The subsequent quantification of Li⁺ diffusion coefficients (D_{Li+}) from these EIS results reveals that the D_{Li+} value of LMNAO experiences a significant drop after 50th and 100th cycles, highlighting how strain accumulation severely degrades ionic transport (Figure 5c). LMNAF maintains coherent lattice integrity between ordered and disordered nanodomains, even at a high delithiation state (4.8 V), with minimal lattice mismatch and negligible strain accumulation. This structural stability ensures the preservation of Li⁺ migration pathways, resulting in a consistently high Li⁺ diffusion ability. In contrast, LMNAO undergoes significant lattice distortion as early as charging to 4.4 V, leading to the progressive formation of antisite defects and a thick rock-salt surface layer upon long-term cycling (Figure 3g,h; Figure S18, Supporting

15214095, 2025, 32, Downloaded from https://advanced

onlinelibrary.wiley.com/doi/10.1002/adma.202418580 by University Town Of Shenzhen, Wiley Online Library on [16/11/2025]. See the Terms.

and Conditions (https://onlinelibrary.wiley

and-conditions) on Wiley Online Library for rules of use; OA articles are governed by the applicable Creative Commons

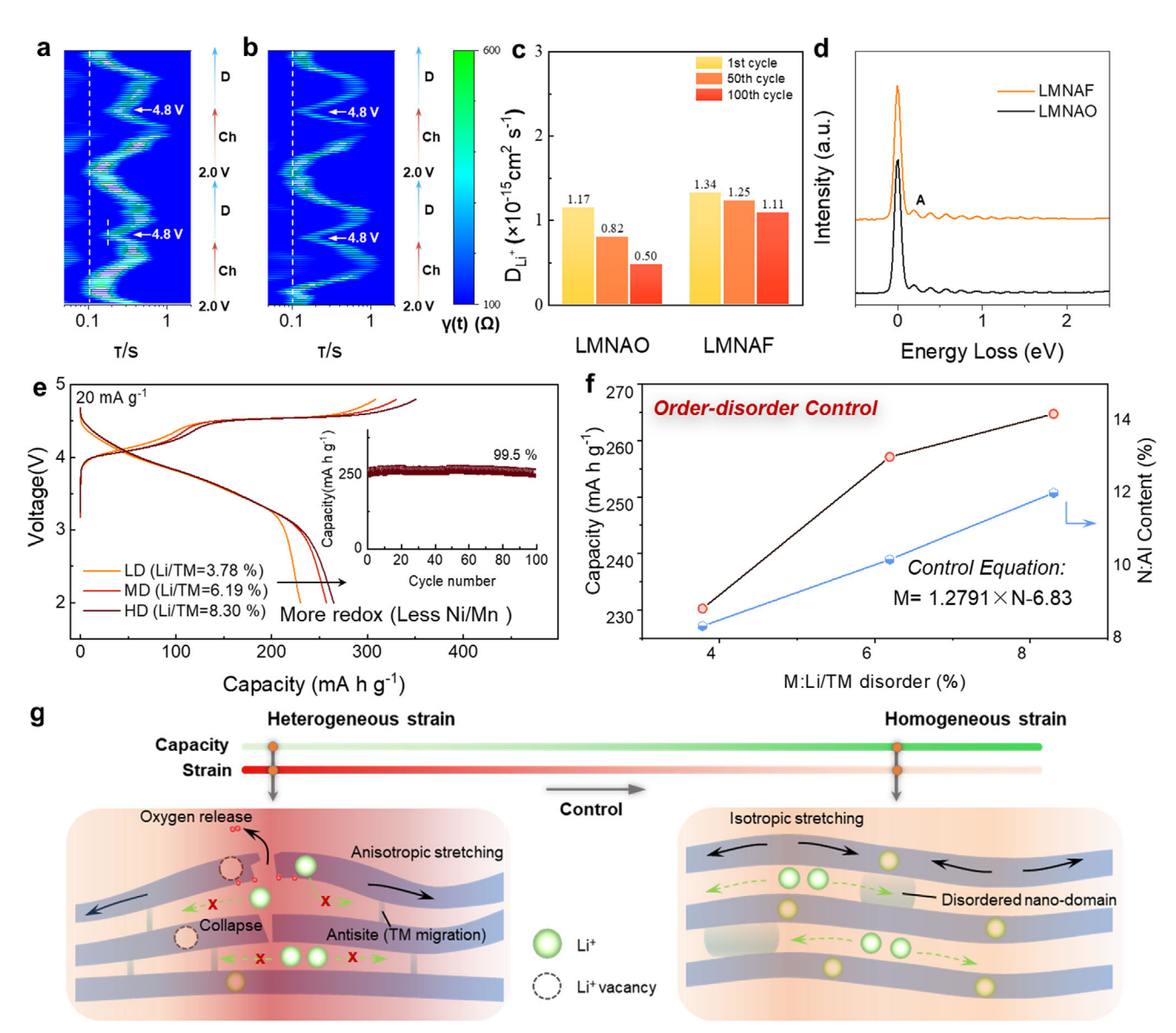


Figure 5. Understanding the role of order–disorder control in Li-rich cathode. a,b) Evolution of charge transfer of LMNAO (a) and LMNAF (b) from the DRT analysis of in situ EIS results during the initial cycles (Ch:charge, D:discharge). c) Comparison of the calculated Li⁺ diffusion coefficients (D_{Li+}) of LNMAF and LNMAO by fitting the EIS results. d) O K-edge RIXS spectra at an excitation energy of 531 eV of LMNAF and LMNAO samples charged to 4.8 V. e) The first charge–discharge voltage profiles of LD, MD, HD at a current density of 20 mA g^{-1} . f) The relationships between capacity and composition as a function of the degree of disorder. g) Schematic illustration of the lattice strain associated with Li⁺ diffusion kinetics and structural degradation process.

Information). Moreover, the resonant inelastic X-ray scattering (RIXS) results further elucidate the critical behavior of oxygen atoms under high-voltage conditions (Figure 5d). The feature associated with oxidized oxygen species (marked as peak A) exhibits similar intensity in both LMNAF and LMNAO, suggesting that no substantial additional formation of molecular O_2 or other newly coordinated oxygen species occurs. This observation suggests that LMNAF maintains a stable oxygen redox environment despite its higher capacity, rather than inducing a shift toward a distinct oxygen coordination environment. [48] In LMNAO, these structural degradations induce severe strain accumulation, obstructing Li⁺ transport and leading to a substantial decline in D_{Li^+}

(Figure 5c). Thus, the stability of the order–disorder structure in LMNAF plays a critical role in mitigating strain-induced degradation, facilitating efficient Li⁺ diffusion, and preserving long-term electrochemical performance.

Regulating the structural order–disorder in cathode materials has long been recognized as a critical handle for performance optimization, [49,50] we expand this strategy to LMR O3-type cathode by incorporating nanosized coherent domains with disordered structure to enhance the electrochemical performance by minimizing lattice strain and enabling a more homogeneous reaction, as demonstrated above. To further demonstrate the generalizability of our strategy, we regulated the proportion of

15214095, 2025, 32, Downloaded from https://advanced.onlinelibrary.wiley.com/doi/10.1002/adma.202418580 by University Town Of Shenzhen, Wiley Online Library on [16/11/2025]. See the Terms and Conditions (https://onlinelibrary.wiley.com/terms-

and-conditions) on Wiley Online Library for rules of use; OA articles are governed by the applicable Creative Commons

electrochemically inert cations (Al) to precisely control the degree of disorder. Two additional compositions with increasing Al content were designed (details provided in the Supporting Information). Rietveld refinement reveals Li/TM disorder (M) values of 3.78%, 6.26%, and 8.74%, respectively (Figure S26 and Tables S5, S6, Supporting Information), which exhibits a strong correlation with the Al content (N) per formula unit. This relationship follows the linear fit $M = 1.2791 \times N - 6.83$ (Figure 5f). Accordingly, we categorize the samples based on their disorder levels as LD (LMNAF), MD, and HD. Despite a decreasing amount of redox active cations and increasing Li/TM disorder, the overall capacity increases from LD (229.0 mAh g⁻¹) to HD (264.7 mAh g⁻¹) (Figure 5e), highlighting that fewer TM ions are involved in the redox process even as capacity increases. This further demonstrates the advantages of coherent order-disorder design for more homogeneous stain distribution, which contributes to a higher capacity. Remarkably, at a high degree of disorder, HD maintains ≈100% capacity retention after 100 cycles at a current density of 20 mA g⁻¹ (Figure 5e inset), with 95% retention at higher rates (Figure S27, Supporting Information).

In a broader context, our design strategy of constructing the coherent order-disorder LMR cathode material is also beneficial for enhancing the sluggish kinetics and provides valuable insights to intrinsically mitigate the voltage hysteresis. The voltage hysteresis phenomenon in Li-rich cathodes is closely related to the anionic redox reaction, [29,51] which is usually accompanied by the TM migration^[52–54] and the irreversible oxygen behavior.^[26,55] The fast kinetics is expected to be achieved by homogeneous lattice strain, including inhibiting cation rearrangement and structural degradation. Micro disorder, i.e., embedded disordered domains, plays a crucial role in mitigating extensive lattice displacements and collective degradation. As depicted in Figure 5g, scattered or isolated antisite defects in layered cathodes without forming aggregated disordered domains are one of the key reasons for capacity decay because they impede Li⁺ migration. In contrast, when antisite defects group together to form local disordered domains with several nanometer length scales, they may serve as a structure stabilizer to avoid significant layer collapse and perturb collective structure degradation because they are thermodynamically more stable with smaller and more isotropic structural strain compared to the layered and spinel phases.^[56,57] The formation of disordered domains does not significantly deteriorate Li⁺ transport, as the recent advancements in cation-disordered cathodes demonstrate facile Li+ transport once with Li-excess compositions (higher than 9% excess).[19] When charged to a high voltage, the embedded disordered phase can perturb the stretching in one direction and provide a smaller, isotropic strain to enhance the structural integrity. The TM migration also alters the Li⁺ diffusion pathways, often resulting in kinetic hindrances and energy density losses.^[58] Macroscopically, this manifests as voltage hysteresis and energy decay. While reversible TM migration contributes to reducing the voltage hysteresis effect to some degree, it will invariably impact Li+ diffusion kinetics. As illustrated in Figure S28 (Supporting Information), TM migration alters the Li⁺ diffusion path. In LMNAF, however, such TM migration can be significantly suppressed, as evidenced by the closeto-zero increase in the Li/TM mixing ratio obtained from XRD Rietveld refinement (Figure 3c). We attribute the reduced TM migration to the homogeneous structural strain, which is confirmed

by electrochemical analysis, as well as the evolution of structure and chemical state during cycling. Additionally, we conducted further analysis on the potential impact of fluorine incorporation in the layered part (Figure S28, Supporting Information), which may contribute to strain reduction. However, its effect is likely limited due to the constrained incorporation of fluorine within the layered domains. [59] Our design strategy effectively inhibits the heterogeneous strain, thereby further preventing TM migration potential molecular O_2 formation (Figure S23, Supporting Information), and subsequent structural and capacity decay.

In the study, we focus on overcoming the critical challenges in the development of O3-type LMR materials for battery applications. Our findings indicate that voltage hysteresis and decay during cycling are primarily governed by Li⁺ diffusion kinetic factors, which can be enhanced by introducing disordered domains to obtain the homogeneous lattice strain. The goal is to emulate the reversible electrochemical redox behaviors seen in NCM and LCO materials by traditional synthesis methods. Order–disorder design and regulation to achieve homogeneity are crucial for advancing next-generation LIB cathode materials that not only enhance performance but also support economic viability and sustainability for practical applications.

4. Conclusion

In summary, we designed, synthesized, and characterized a cobalt-free LMR cathode featuring coherent order—disordered nanodomains. This unique structure effectively alleviates the heterogeneous strain commonly encountered during cycling, thereby enhancing both cycling stability and energy density. The enhanced Li⁺ diffusion kinetics are proposed to originate from the perturbation of unidirectional stretching and mitigated TM migration. Moreover, order—disorder control enables a homogeneous structural evolution of O3-type cathode materials, thereby elevating stability and enabling more reversible Li extraction—insertion. This strategy significantly provides valuable insights for the advancement of Li-rich layered cathodes and highlights the importance of short-range order—disorder tuning for energy storage materials.

5. Experimental Section

Synthesis: LMNAF and LMNAO precursors were synthesized via the sol-gel method, based on the designed molecular formulas spectively. The following raw materials were accurately measured for LMNAF: 2.102 g of C₂H₃O₂Li•2H₂O (99%, Aladin), 0.838 g of C₄H₆O₄Ni•4H₂O (99%, Aladin), 2.476 g of C₄H₆O₄Mn•4H₂O (99%, Aladin), 0.273 g of Al(OH)(CH3COO)2 (99%, Aladin), and 0.130 g of LiF (100%, Aladin). Citric acid (100%, Aladdin) and polyvinylpyrrolidone (PVP-K30, 100%, Sinopharm Chemical Reagent Co., Ltd.) were used as complexing agents in a 1:3 ratio, maintaining a 2:1 molar ratio of complexing agent to transition metals. In the precursor synthesis, LiF was initially added to a crucible, followed by a measured quantity of dilute nitric acid. Then, the remaining materials were sequentially incorporated. The mixture was subjected to a 90 °C oil bath after adding an appropriate volume of deionized water. The LMNAO precursor was prepared using identical steps, except for omitting LiF with C₂H₃O₂Li•2H₂O.

The solution was continuously stirred in the oil bath until it formed a gel. It was then transferred to a muffle furnace and annealed at a ramp

15214995, 2025, 32, Downloaded from https://advanced.onlinelibrary.wiley.com/doi/10.1002/adma.202418580 by University Town Of Shenzhen, Wiley Online Library on [161112025]. See the Terms and Conditions (https://onlinelibrary.wiley.com/terms-and-conditions) on Wiley Online Library for rules of use; OA ariseks are governed by the applicable Cerative Commons

rate of 5 °C min⁻¹, first at 140 °C for 3 h and subsequently at 500 °C for another 3 h to obtain the precursor. The annealed material was ground into a fine powder using an agate mortar. This powder was then calcined in an O_2 atmosphere at a heating rate of 3 °C min⁻¹, culminating in a final temperature of 800 °C for 10 h. The final LMNAO and LMNAF powders were obtained by filtering the resultant powders twice with deionized water to remove impurities, followed by drying in an oven for 12 h to eliminate any residual moisture.

Electrochemistry: Electrochemical measurements were conducted using Coin-type (CR2032) half cells. The active materials, polyvinylidene fluoride (PVDF, Solvay 5130), and carbon black (C45 Conductive Carbon Black, TIMCAL) were mixed in n-methyl-2-pyrrolidone (NMP) in a weight ratio of 7:2:1. This mixture was stirred at 2000 rpm for 20 min using a THINKY AR-100 mixer to create a uniform slurry. The slurry was then applied onto Al foil and dried in a vacuum at 80 $^{\circ}$ C for 8 h. The active loading was 1.8 mg cm $^{-2}$. As the electrolyte, a 1.2 M LiPF₆ solution in an EC/EMC (3:7) mixed solvent with 5% FEC was used. Galvanostatic charge-discharge tests were carried out on a NEWARE battery testing system (MIHW-200-160CH, where 1 C = 200 mA g^{-1}) at 25 °C. Ex situ electrochemical impedance spectroscopy of the coin cells was performed at various cycle numbers, ranging from 10^5 to 10^{-1} Hz with a 10 mV voltage amplitude, using a Solartron 1400 cell test system. The charge transfer of DRT was characterized by in situ EIS measurements, which were performed using an SP-50e Potentiostat. The frequency for these measurements was set to range from 1 MHz to 0.1 Hz, with an amplitude fixed at 10 mV. Galvanostatic electrochemical impedance spectroscopy (GEIS) measurements were consistently conducted at regular intervals during both charging and discharging cycles. Each measurement was taken after maintaining a stable voltage for 30 min, with a set voltage interval of 0.1 V. For the analysis of the DRT, MATLAB software, developed by the research team led by Ciucci, [60] was employed.

Characterization: X-ray powder diffraction data for cathode materials were gathered using synchrotron XRD at the 11-ID-C sector of the Advanced Photon Source at Argonne National Laboratory. A high-energy X-ray beam, measuring 0.2 mm by 0.2 mm and with a wavelength of 0.1173 Å, was employed to produce 2D diffraction patterns using transmission geometry. These patterns were recorded on a Perkin-Elmer largearea detector, positioned 1800 mm from the samples. Neutron powder diffraction data of the backward scattering bank, the medium-angle bank, and the low-angle bank were collected at the time-of-flight (TOF) diffractometer General Purpose Powder Diffractometer (GPPD) at China Spallation Neutron Source (CSNS). The synchrotron XRD and ND patterns were analyzed through combined Rietveld refinement using the TOPAS software. X-ray total scattering data were collected at beamline 11-ID-C of the Advanced Photon Source in Argonne National Laboratory for PDF analysis. The refinement of PDF data was conducted using the PDFgui software.^[61] The atomically resolved HAADF-STEM images were carried out on an aberration-corrected scanning transmission electron microscope (FEI Tian Themis 60-300 kV, operated at 300 kV). TEM samples were prepared using the focused ion beam (FIB, Scios 2 DualBeam). HRTEM, TEM-EDX, and SAED mapping were conducted using the JEOL-3200FS Field Emission Transmission Electron Microscope (FETEM) operating at 300 kV. ToF-SIMS measurements were performed at TESCAN, achieving a depth resolution finer than 3 nm. XPS measurements were carried out using a Thermo Scientific Escalab 250Xi spectrometer. In situ XRD of LM-NAF was performed at the Shenzhen Institute of Advanced Science Facilities (IASF) with a liquid metal jet source (Ga Kα: 9.24 keV, wavelength: 1.3418 Å) and a Dectris Pilatus 1 м detector. In situ XRD of LMNAO was performed at Argonne National Laboratory. sXAS measurements were conducted at the Shanghai Synchrotron Radiation Facility (SSRF), utilizing BL02B02 of the SiP·ME². These measurements were performed using both TEY and TFY detection methods. The experiment achieved a photon flux of 1011 photons per second and an energy resolving power . (E/ Δ E) of 13000 at 250 eV. Operando differential electrochemical mass spectrometry (DEMS) measurements were conducted using a custombuilt DEMS apparatus. The cells within the DEMS setup were allowed to stabilize for a duration of 1 h. Following this stabilization period, galvanostatic charging was executed employing a NEWARE electrochemical workstation. XANES measurements were performed using QuantumLeap H2000. RIXS measurements were performed at the U41-PEAXIS beamline at BESSY II, Helmholtz–Zentrum Berlin (HZB). $^{[62]}$ The samples were transferred from an $\rm N_2$ -filled glovebox to the experimental chamber. The spectrometer was aligned at specular conditions with a scattering angle of 60° and optimized to achieve a combined energy resolution of 90 meV, calibrated using carbon tape. RIXS spectra at the O K-edge were collected with an excitation energy of 531.0 eV.

Computation: DFT calculations were conducted to calculate the formation energies of the Li[Li $_{1/4}$ Mn $_{1/2}$ Ni $_{1/6}$ Al $_{1/12}$]O $_{1.75}$ Fo $_{0.25}$ cathode materials as a function of the average number of Li—F bonds around a F ion in the structure. The DFT-calculated energies averaged over 48 different structures with different number of Li—F/TM—F bonds. These variations involved random exchanges of the positions of the cations in the transition metal layer and the anions. All the calculations were performed by using the projector-augmented wave (PAW) method[$^{63-65}$] as implemented in the Vienna Ab initio Simulation Package (VASP). [66] A rotationally averaged Hubbard U correction[67] was performed to correct the self-interaction error. The Hubbard U parameters were derived from a calibration previously established for oxide formation energies, as reported in earlier literature. $^{(68)}$ For all the calculations, a reciprocal space discretization of 25 k-points per Å $^{-1}$ was applied, and the convergence criteria were set as $^{10-6}$ eV for electronic loops and $^{0.02}$ eVÅ $^{-1}$ for ionic loops.

Supporting Information

Supporting Information is available from the Wiley Online Library or from the author

Acknowledgements

This work was financially supported by the National Natural Science Foundation of China (52172175), the Shenzhen Science and Technology Research Grant (JCYJ20210324130812033), the Program from Guangdong Introducing Innovative and Entrepreneurial Teams (2019ZT08L101 and RCTDPT-2020-001), the Basic and Applied Basic Research Foundation of Guangdong Province (No. 2021B1515130002), the Soft Science Research Project of Guangdong Province (No. 2017B030301013), the Shenzhen Science and Technology Research Grant (No. ZDSYS201707281026184), the Chemistry and Chemical Engineering Guangdong Laboratory (1922018), the National Natural Science Foundation of China (No. 22479148). The authors gratefully acknowledge funding support from the Fundamental Research Funds for the Central Universities. The calculations were carried out on the ORISE Supercomputer. The authors acknowledge support from the US Department of Energy (DOE), Office of Energy Efficiency and Renewable Energy, Vehicle Technologies Office. This work was also supported by the Clean Vehicles, US-China Clean Energy Research Centre (CERC-CVC2) under the US DOE EERE Vehicle Technologies Office. Argonne National Laboratory is operated for the DOE Office of Science by UChicago Argonne, LLC, under contract number DE-AC02-06CH11357. [Correction added on May 24, 2025, after first online publication: Figure 1 has been updated.]

Conflict of Interest

The authors declare no conflict of interest.

Author Contributions

S.X., Z.G., and H.C. contributed equally to this work. S.X. and G.Z. conceived the idea and designed the experiments. S.X. and G.Z. synthesized all the materials and conducted electrochemical measurements. S.X. and L.C. conducted TEM and STEM experiments and related data analysis.



www.advancedsciencenews.com

ADVANCED MATERIALS

www.advmat.de

15214095, 2025, 32, Downloaded from https://advanced.onlinelibrary.wiley.com/doi/10.1002/adma.202418580 by University Town Of Sherzhen, Wiley Online Library on [16/11/2025]. See the Terms and Conditions (https://onlinelibrary.wiley.a

on Wiley Online Library for rules of use; OA articles are governed by the applicable Creative Commons

S.X., N.Z., H.X., Q.L., and M.Z. conducted the XAS experiments and analysis. D.Z., T.L., S.X., G.Z., W.H., C.L., and T.L. performed ex situ synchrotron PDF, XRD, and in situ XRD. S.X., M.Z., and L.H. conducted ND experiments. S.X. and T.W. performed the combined refinement and analysis. Z.L., H.C., and S.X. conducted DFT calculations. S.X., Z.L. wrote the manuscript, and all authors edited the manuscript. Z.L., M.Z., and F.P. supervised the work. All authors discussed the results and commented on the manuscript.

Data Availability Statement

The data that support the findings of this study are available from the corresponding author upon reasonable request.

Keywords

homogenous, lattice strain, Li-rich cathode, Mn-based cathode, order-disorder control

Received: November 28, 2024 Revised: May 13, 2025 Published online: May 21, 2025

- [1] G. Assat, J.-M. Tarascon, Nat. Energy 2018, 3, 373.
- [2] M. M. Rahman, F. Lin, Matter 2021, 4, 490.
- [3] Y. Dong, J. Li, Chem. Rev. 2023, 123, 811.
- [4] T. Liu, J. Liu, L. Li, L. Yu, J. Diao, T. Zhou, S. Li, A. Dai, W. Zhao, S. Xu, Y. Ren, L. Wang, T. Wu, R. Qi, Y. Xiao, J. Zheng, W. Cha, R. Harder, I. Robinson, J. Wen, J. Lu, F. Pan, K. Amine, *Nature* 2022, 606, 305.
- [5] S. Xu, Z. Chen, W. Zhao, W. Ren, C. Hou, J. Liu, W. Wang, C. Yin, X. Tan, X. Lou, X. Yao, Z. Gao, H. Liu, L. Wang, Z. Yin, B. Qiu, B. Hu, T. Li, C. Dong, F. Pan, M. Zhang, *Energy Environ. Sci.* 2024, 17, 3807.
- [6] P. Yan, J. Zheng, Z. K. Tang, A. Devaraj, G. Chen, K. Amine, J. G. Zhang, L. M. Liu, C. Wang, Nat. Nanotechnol. 2019, 14, 602.
- [7] E. Hu, X. Yu, R. Lin, X. Bi, J. Lu, S. Bak, K.-W. Nam, H. L. Xin, C. Jaye, D. A. Fischer, K. Amine, X.-Q. Yang, Nat. Energy 2018, 3, 690.
- [8] E. Lee, K. A. Persson, Adv. Energy Mater. 2014, 4, 2001671.
- [9] S. Kim, M. Aykol, V. I. Hegde, Z. Lu, S. Kirklin, J. R. Croy, M. M. Thackeray, C. Wolverton, Energy Environ. Sci. 2017, 10, 2201.
- [10] W. Huang, T. Liu, L. Yu, J. Wang, T. Zhou, J. Liu, T. Li, R. Amine, X. Xiao, M. Ge, L. Ma, S. N. Ehrlich, M. V. Holt, J. Wen, K. Amine, *Science* 2024, 384, 912.
- [11] Z. Cai, B. Ouyang, H.-M. Hau, T. Chen, R. Giovine, K. P. Koirala, L. Li, H. Ji, Y. Ha, Y. Sun, J. Huang, Y. Chen, V. Wu, W. Yang, C. Wang, R. J. Clément, Z. Lun, G. Ceder, *Nat. Energy* 2024, 9, 27.
- [12] S. Zhao, K. Yan, J. Zhang, B. Sun, G. Wang, Angew. Chem. Int. Ed. 2021, 60, 2208.
- [13] D. Luo, H. Zhu, Y. Xia, Z. Yin, Y. Qin, T. Li, Q. Zhang, L. Gu, Y. Peng, J. Zhang, K. M. Wiaderek, Y. Huang, T. Yang, Y. Tang, S. Lan, Y. Ren, W. Lu, C. M. Wolverton, Q. Liu, *Nat. Energy* **2023**, *8*, 1078.
- [14] D. Eum, B. Kim, S. J. Kim, H. Park, J. Wu, S. P. Cho, G. Yoon, M. H. Lee, S. K. Jung, W. Yang, W. M. Seong, K. Ku, O. Tamwattana, S. K. Park, I. Hwang, K. Kang, *Nat. Mater.* 2020, *19*, 419.
- [15] F. Wu, J. Maier, Y. Yu, Chem. Soc. Rev. 2020, 49, 1569.
- [16] Y. Cao, M. Li, J. Lu, J. Liu, K. Amine, Nat. Nanotechnol. 2019, 14, 200.
- [17] J. W. Choi, D. Aurbach, Nat. Rev. Mater. 2016, 1, 16013.
- [18] C. Lin, J. Li, Z. W. Yin, W. Huang, Q. Zhao, Q. Weng, Q. Liu, J. Sun, G. Chen, F. Pan, Adv. Mater. 2023, 36, 2307404.
- [19] J. Lee, A. Urban, X. Li, D. Su, G. Hautier, G. Ceder, Science 2014, 343, 519.
- [20] Z. Cai, H. Ji, Y. Ha, J. Liu, D.-H. Kwon, Y. Zhang, A. Urban, E. E. Foley, R. Giovine, H. Kim, Z. Lun, T.-Y. Huang, G. Zeng, Y. Chen, J. Wang, B.

- D. Mccloskey, M. Balasubramanian, R. J. Clément, W. Yang, G. Ceder, *Matter* **2021**, *4*, 3897.
- [21] H. Ji, J. Wu, Z. Cai, J. Liu, D.-H. Kwon, H. Kim, A. Urban, J. K. Papp, E. Foley, Y. Tian, M. Balasubramanian, H. Kim, R. J. Clément, B. D. Mccloskey, W. Yang, G. Ceder, *Nat. Energy* 2020, 5, 213.
- [22] K. Luo, M. R. Roberts, N. Guerrini, N. Tapia-Ruiz, R. Hao, F. Massel, D. M. Pickup, S. Ramos, Y. S. Liu, J. Guo, A. V. Chadwick, L. C. Duda, P. G. Bruce, J. Am. Chem. Soc. 2016, 138, 11211.
- [23] K. Luo, M. R. Roberts, R. Hao, N. Guerrini, D. M. Pickup, Y.-S. Liu, K. Edstrom, J. Guo, A. V. Chadwick, L. C. Duda, P. G. Bruce, *Nat. Chem.* 2016, 8, 684.
- [24] B. Li, Z. Zhuo, L. Zhang, A. Iadecola, X. Gao, J. Guo, W. Yang, A. V. Morozov, A. M. Abakumov, J. M. Tarascon, *Nat. Mater.* 2023, 22, 1370.
- [25] R. A. House, U. Maitra, M. A. Perez-Osorio, J. G. Lozano, L. Jin, J. W. Somerville, L. C. Duda, A. Nag, A. Walters, K. J. Zhou, M. R. Roberts, P. G. Bruce, *Nature* 2020, 577, 502.
- [26] R. A. House, G. J. Rees, M. A. Pérez-Osorio, J.-J. Marie, E. Boivin, A. W. Robertson, A. Nag, M. Garcia-Fernandez, K.-J. Zhou, P. G. Bruce, Nat. Energy 2020, 5, 777.
- [27] J. H. Song, S. Yu, B. Kim, D. Eum, J. Cho, H. Y. Jang, S. O. Park, J. Yoo, Y. Ko, K. Lee, M. H. Lee, B. Kang, K. Kang, *Nat. Commun.* 2023, 14, 4149.
- [28] K. Mccoll, R. A. House, G. J. Rees, A. G. Squires, S. W. Coles, P. G. Bruce, B. J. Morgan, M. S. Islam, *Nat. Commun.* 2022, 13, 5275.
- [29] J. Hong, W. E. Gent, P. Xiao, K. Lim, D. H. Seo, J. Wu, P. M. Csernica, C. J. Takacs, D. Nordlund, C. J. Sun, K. H. Stone, D. Passarello, W. Yang, D. Prendergast, G. Ceder, M. F. Toney, W. C. Chueh, *Nat. Mater.* 2019, 18 256
- [30] M. J. Hÿtch, E. Snoeck, R. Kilaas, Ultramicroscopy 1998, 74, 131.
- [31] F. Lin, I. M. Markus, D. Nordlund, T.-C. Weng, M. D. Asta, H. L. Xin, M. M. Doeff, *Nat. Commun.* **2014**, *5*, 3529.
- [32] E. C. Wasinger, F. M. F. De Groot, B. Hedman, K. O. Hodgson, E. I. Solomon, J. Am. Chem. Soc. 2003, 125, 12894.
- [33] R. Qiao, T. Chin, S. J. Harris, S. Yan, W. Yang, Curr. Appl. Phys. 2013, 13, 544.
- [34] W. Yang, T. P. Devereaux, J. Power Sources 2018, 389, 188.
- [35] A. Ito, Y. Sato, T. Sanada, M. Hatano, H. Horie, Y. Ohsawa, J. Power Sources 2011, 196, 6828.
- [36] J. Rana, J. K. Papp, Z. Lebens-Higgins, M. Zuba, L. A. Kaufman, A. Goel, R. Schmuch, M. Winter, M. S. Whittingham, W. Yang, B. D. Mccloskey, L. F. J. Piper, ACS Energy Lett. 2020, 5, 634.
- [37] R. Qiao, L. A. Wray, J.-H. Kim, N. P. W. Pieczonka, S. J. Harris, W. Yang, J. Phys. Chem. C 2015, 119, 27228.
- [38] Z. Zhu, D. Yu, Y. Yang, C. Su, Y. Huang, Y. Dong, I. Waluyo, B. Wang, A. Hunt, X. Yao, J. Lee, W. Xue, J. Li, *Nat. Energy* 2019, 4, 1049.
- [39] H. Liu, W. Hua, S. Kunz, M. Bianchini, H. Li, J. Peng, J. Lin, O. Dolotko, T. Bergfeldt, K. Wang, C. Kubel, P. Nagel, S. Schuppler, M. Merz, B. Ying, K. Kleiner, S. Mangold, D. Wong, V. Baran, M. Knapp, H. Ehrenberg, S. Indris, *Nat. Commun.* 2024, 15, 9981.
- [40] S. Hy, W.-N. Su, J.-M. Chen, B.-J. Hwang, J. Phys. Chem. C 2012, 116, 25242.
- [41] W.-S. Yoon, K.-B. Kim, M.-G. Kim, M.-K. Lee, H.-J. Shin, J.-M. Lee, J.-S. Lee, C.-H. Yo, J. Phys. Chem. B 2002, 106, 2526.
- [42] J. Xu, M. Sun, R. Qiao, S. E. Renfrew, L. Ma, T. Wu, S. Hwang, D. Nordlund, D. Su, K. Amine, J. Lu, B. D. Mccloskey, W. Yang, W. Tong, Nat. Commun. 2018, 9, 947.
- [43] S. Xu, X. Tan, W. Ding, W. Ren, Q. Zhao, W. Huang, J. Liu, R. Qi, Y. Zhang, J. Yang, C. Zuo, H. Ji, H. Ren, B. Cao, H. Xue, Z. Gao, H. Yi, W. Zhao, Y. Xiao, Q. Zhao, M. Zhang, F. Pan, Angew. Chem., Int. Ed. 2023, 62, 202218595.
- [44] Q. Y. Li, D. Ning, D. Wong, K. An, Y. X. Tang, D. Zhou, G. Schuck, Z. H. Chen, N. A. Zhang, X. F. Liu, Nat. Commun. 2022, 13, 1123.

15214095, 2025, 32, Downloaded from https://advanced.onlinelibrary.wiley.com/doi/10.1002/adma.202418580 by University Town Of Shenzhen, Wiley Online Library on [16/11/2025]. See the Terms

and Conditions

for rules of use; OA

articles are governed by the applicable Creative Commons

- [45] J. Ahn, D. Chen, G. Chen, Adv. Energy Mater. 2020, 10, 2001671.
- [46] D. Leanza, C. A. F. Vaz, P. Novak, M. El Kazzi, Helv. Chim. Acta 2020, 104, 2000183.
- [47] Y. Lu, C. Zhao, J. Huang, Q. Zhang, Joule 2022, 6, 1172.
- [48] X. Gao, B. Li, K. Kummer, A. Geondzhian, D. A. Aksyonov, R. Dedryvere, D. Foix, G. Rousse, M. Ben Yahia, M. L. Doublet, A. M. Abakumov, J. M. Tarascon, *Nat. Mater.* 2025, 24, 743.
- [49] Q. Wang, Z. Yao, J. Wang, H. Guo, C. Li, D. Zhou, X. Bai, H. Li, B. Li, M. Wagemaker, C. Zhao, *Nature* 2024, 629, 341.
- [50] Q. Zhao, F. Pan, Joule 2024, 8, 2187.
- [51] G. Assat, D. Foix, C. Delacourt, A. Iadecola, R. Dedryvere, J. M. Tarascon, Nat. Commun. 2017, 8, 2219.
- [52] W. E. Gent, K. Lim, Y. Liang, Q. Li, T. Barnes, S. J. Ahn, K. H. Stone, M. Mcintire, J. Hong, J. H. Song, Y. Li, A. Mehta, S. Ermon, T. Tyliszczak, D. Kilcoyne, D. Vine, J. H. Park, S. K. Doo, M. F. Toney, W. Yang, D. Prendergast, W. C. Chueh, *Nat. Commun.* 2017, 8, 2091.
- [53] J. Huang, B. Ouyang, Y. Zhang, L. Yin, D. H. Kwon, Z. Cai, Z. Lun, G. Zeng, M. Balasubramanian, G. Ceder, Nat. Mater. 2023, 22, 353.
- [54] K. Ku, B. Kim, S.-K. Jung, Y. Gong, D. Eum, G. Yoon, K.-Y. Park, J. Hong, S.-P. Cho, D.-H. Kim, H. Kim, E. Jeong, L. Gu, K. Kang, Energy Environ. Sci. 2020, 13, 1269.
- [55] R. A. House, J.-J. Marie, M. A. Pérez-Osorio, G. J. Rees, E. Boivin, P. G. Bruce, *Nat. Energy* **2021**, *6*, 781.

- [56] N. Li, M. Sun, W. H. Kan, Z. Zhuo, S. Hwang, S. E. Renfrew, M. Avdeev, A. Huq, B. D. Mccloskey, D. Su, W. Yang, W. Tong, *Nat. Commun.* 2021, 12, 2348.
- [57] W. B. Hua, S. N. Wang, M. Knapp, S. J. Leake, A. Senyshyn, C. Richter, M. Yavuz, J. R. Binder, C. P. Grey, H. Ehrenberg, S. Indris, B. Schwarz, Nat. Commun. 2019, 10, 5365.
- [58] G. Assat, S. L. Glazier, C. Delacourt, J.-M. Tarascon, Nat. Energy 2019, 4, 647.
- [59] W. D. Richards, S. T. Dacek, D. A. Kitchaev, G. Ceder, Adv. Energy Mater. 2017, 8, 1701533.
- [60] T. H. Wan, M. Saccoccio, C. Chen, F. Ciucci, Electrochim. Acta 2015, 184, 483.
- [61] C. Farrow, P. Juhas, J. Liu, D. Bryndin, E. Božin, J. Bloch, T. Proffen, S. Billinge, J. Phys., Condens. Matter 2007, 19, 335219.
- [62] C. Schulz, K. Lieutenant, J. Xiao, T. Hofmann, D. Wong, K. Habicht, J. Synchrotron Radiat. 2020, 27, 238.
- [63] G. Kresse, D. Joubert, Phys. Rev. B 1999, 59, 1758.
- [64] P. E. Blöchl, Phys. Rev. B 1994, 50, 17953.
- [65] J. P. Perdew, K. Burke, M. Ernzerhof, Phys. Rev. Lett. 1996, 77, 3865.
- [66] G. Kresse, J. Hafner, Phys. Rev. B 1993, 47, 558.
- [67] S. L. Dudarev, G. A. Botton, S. Y. Savrasov, C. J. Humphreys, A. P. Sutton, *Phys. Rev. B* 1998, *57*, 1505.
- [68] L. Wang, T. Maxisch, G. Ceder, Phys. Rev. B 2006, 73, 195107.